Volume 6 | Number 42 | 14 November 2018 | Pages 20525–21232

Journal of Materials Chemistry A

Materials for energy and sustainability

rsc.li/materials-a

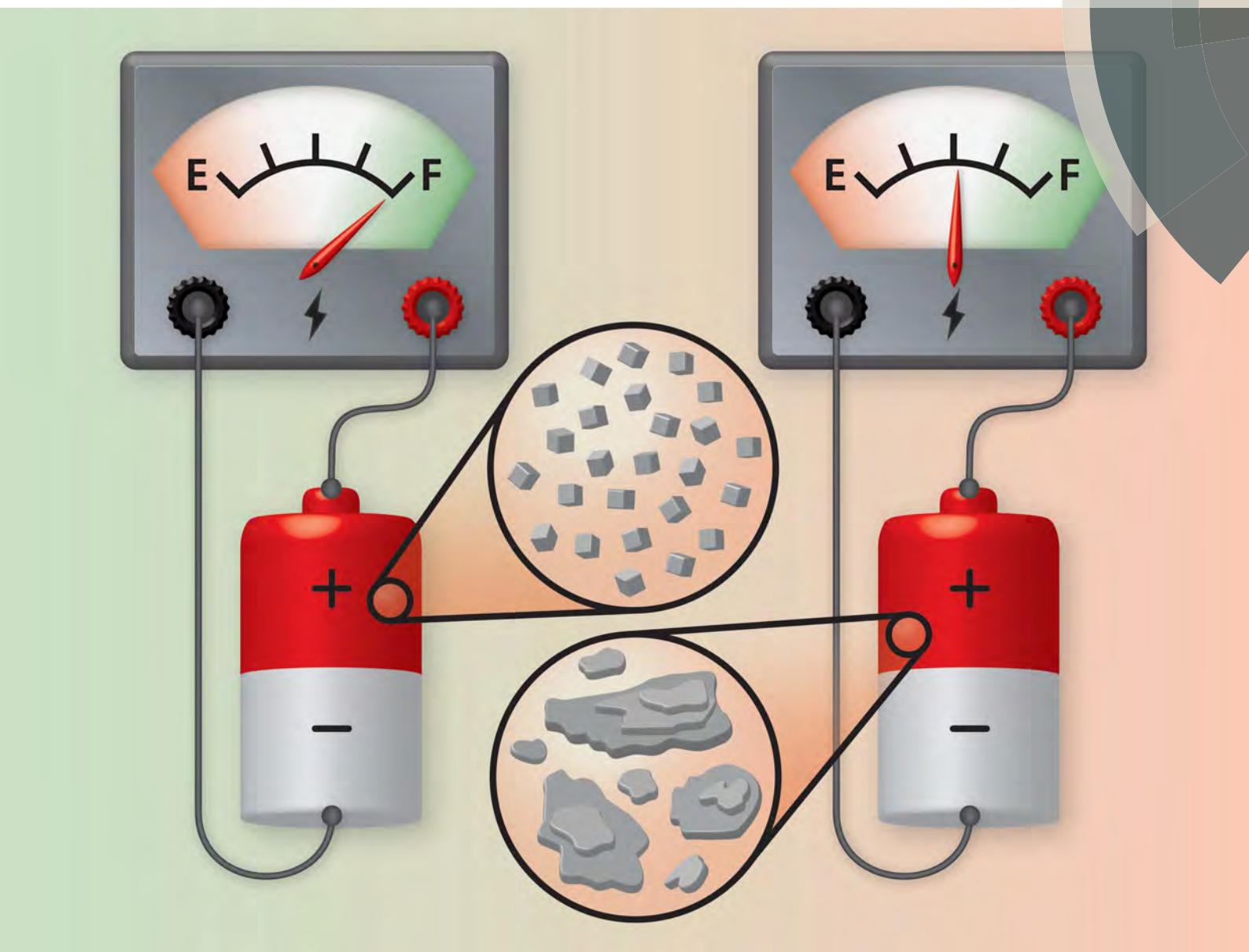

ISSN 2050-7488

ROYAL SOCIETY OF CHEMISTRY

PAPER

Louis F. J. Piper *et al.*

Role of disorder in limiting the true multi-electron redox in ε-$LiVOPO_4$

Journal of Materials Chemistry A

PAPER

Cite this: J. Mater. Chem. A, 2018, 6, 20669

Role of disorder in limiting the true multi-electron redox in ε-$LiVOPO_4$†

Jatinkumar Rana,[a] Yong Shi,[a] Mateusz J. Zuba,[a] Kamila M. Wiaderek,[b] Jun Feng,[a] Hui Zhou,[a] Jia Ding,[a] Tianpin Wu,[b] Giannantonio Cibin,[c] Mahalingam Balasubramanian,[b] Fredrick Omenya,[a] Natasha A. Chernova,[a] Karena W. Chapman,[d] M. Stanley Whittingham[a] and Louis F. J. Piper*[a]

Received 5th July 2018
Accepted 7th September 2018

DOI: 10.1039/c8ta06469e

rsc.li/materials-a

Recent advances in materials syntheses have enabled ε-$LiVOPO_4$ to deliver capacities approaching, and in some cases exceeding the theoretical value of 305 mA h g^{-1} for 2Li intercalation, despite its poor electronic and ionic conductivity. However, not all of the capacity corresponds to the true electrochemical intercalation/deintercalation reactions as evidenced upon systematic tracking of V valence through combined operando and rate-dependent *ex situ* X-ray absorption study presented herein. Structural disorder and defects introduced in the material by high-energy ball milling impede kinetics of the high-voltage V^{5+}/V^{4+} redox more severely than the low-voltage V^{4+}/V^{3+} redox, promoting significant side reaction contributions in the high-voltage region, irrespective of cycling conditions. The present work emphasizes the need for nanoengineering of active materials without compromising their bulk structural integrity in order to fully utilize high-energy density of multi-electron cathode materials.

Introduction

Currently, the energy density of Li-ion batteries is limited by cathode chemistries, with layered $LiCoO_2$ (ref. 1) and olivine $LiFePO_4$ (ref. 2) being the most commonly used cathodes. However, only ~0.5Li per mole of $LiCoO_2$ can be safely utilized,[3] which limits its energy density to 520 W h kg^{-1}. The efforts are ongoing to push this limit further by partial substitution of Co with Mn, Ni and Al, giving rise to materials commonly referred to as NMC[4] and NCA,[5] in addition to exploring anionic redox activities.[6–9] $LiFePO_4$, on the other hand, offers improved safety and stable capacity of ~170 mA h g^{-1} on cycling. These advantages are, however, offset by an increase in the weight due to heavier PO_4 groups and a lower operating voltage (~3.4 V *vs.* Li/Li^+) which cap the energy density of $LiFePO_4$ at 586 W h kg^{-1}.[3] One way of overcoming the current limitations on energy density is to explore cathode chemistries capable of multi-electron transfer per transition-metal redox center.

To that end, vanadyl phosphates seem attractive as V can assume a variety of oxidation states ranging from 2+ to 5+. Since Lim *et al.*[10] first examined the possibility of multi-electron redox in vanadyl phosphates, various polymorphs of $VOPO_4$ have been investigated as candidate cathodes for Li-ion batteries.[3,11–31] Following the work of Azmi *et al.*[14] which demonstrated the ε polymorph with triclinic structure (often referred to as α polymorph in some literature[13,25,28]) as the promising candidate, both ε-$VOPO_4$ and its lithiated counterpart, ε-$LiVOPO_4$, have received increased attention of the battery community. However, most of the literature concerning ε-$LiVOPO_4$ is either focused at achieving reversible intercalation of the second Li (*i.e.*, ε-$Li_{1+x}VOPO_4$ with $0 \leq x \leq 1$) in the low-voltage region of 1.6–3.5 V or that of the first Li (*i.e.*, ε-Li_xVOPO_4 with $0 \leq x \leq 1$) in the high-voltage region of 3.0–4.5 V, separately.[11,20,21,23,24,27,28,32,33] It should be noted that achieving full capacity corresponding to 1Li either in the low- or high-voltage region would render vanadyl phosphates only at par with the currently existing $LiFePO_4$ or layered $LiMO_2$ (M = Ni, Mn, Co, Al) at best, and any efforts in exploring/optimizing vanadyl phosphates are justified only if reversible intercalation of 2Li in the full-voltage range of 1.6–4.5 V which corresponds to the energy density of ~900 W h kg^{-1}, is realized. Multi-electron redox in ε-$LiVOPO_4$ has not been explored until very recently[28,31] due to poor electronic and ionic conductivity of the material,[21] for which, nanosizing of active particles *via* high-energy ball milling is recommended,[11,13,17,31] but success is limited.[34] In contrast, ε-$VOPO_4$ has demonstrated encouraging electrochemical performance for multi-electron transfer since the beginning[16,22,26,30,35,36] and recently, Whittingham and coworkers achieved the full theoretical capacity for reversible intercalation of 2Li in

[a]NorthEast Center for Chemical Energy Storage (NECCES) at Binghamton University in Binghamton, NY, 13902, USA. E-mail: lpiper@binghamton.edu

[b]X-ray Science Division, Advanced Photon Source, Argonne National Laboratory, Argonne, Illinois 60439, USA

[c]Diamond Light Source Ltd., Diamond House, Harwell Science and Innovation Campus, Didcot, Oxfordshire OX11 0DE, UK

[d]Department of Chemistry, Stony Brook University, Stony Brook, New York 11974, USA

† Electronic supplementary information (ESI) available. See DOI: 10.1039/c8ta06469e

hydrothermally-synthesized ε-$VOPO_4$.[37] This leads to an intriguing question as to what enables the full multi-electron redox in ε-$VOPO_4$, but not in ε-$LiVOPO_4$ when both materials essentially follow similar reaction pathways during electrochemical cycling.

In the present work, we exploit the element-selective nature of X-ray absorption spectroscopy (XAS) to investigate the factors limiting multi-electron redox in solid-state-synthesized ε-$LiVOPO_4$. Our results highlight the role of high-energy ball milling in limiting the true multi-electron redox and promoting interfacial side reactions in ε-$LiVOPO_4$, irrespective of cycling conditions. By systematically tracking the evolution of V valence and local structure for various states of discharge/charge through combined operando and rate-dependent *ex situ* investigation, we were able to separate the contributions of true V redox from those of side reactions. We further investigated the implications of these side reactions on the long-term cycling performance of the material by examining cycled samples.

Experimental

ε-$LiVOPO_4$ was synthesized by a solid-state method using Li_2CO_3 (Sigma-Aldrich, ≥99.0), NH_4VO_3 (Sigma-Aldrich, 99.0) and $NH_4H_2PO_4$ (Sigma-Aldrich, ≥99.99) in a stoichiometric ratio of Li : V : P as 1 : 1 : 1. The precursors were subjected to planetary ball milling (Across International, PQ-N04) in acetone for 4 h. After drying, the powder was pressed into pellets and heated to 300 °C for 5 h in an argon atmosphere to remove ammonia. The solid mixture was again heated to 800 °C for 10 h in an argon atmosphere to form ε-$LiVOPO_4$. The as-synthesized ε-$LiVOPO_4$ was subjected to high-energy ball milling (SPEX, 8000D) with acetylene black (Alfa Aesar, 100%) for 0.5 h. Ball milling was carried out at a speed of 2000 rpm using six small balls (1 g each) and two big balls (8 g each). A typical ball milling batch involved 0.5 g of ε-$LiVOPO_4$, leading to the balls-to-ε-$LiVOPO_4$ weight ratio of 44 : 1. The resultant mixture of ε-$LiVOPO_4$ and acetylene black was then mixed with polyvinylidene difluoride (PVDF) binder (Sigma-Aldrich) using 1-methyl-2-pyrrolidinone (NMP) as the solvent. The weight ratio of ε-$LiVOPO_4$: acetylene black : PVDF was maintained as 75 : 15 : 10. The resultant slurry was tape-cast on an aluminum current collector and dried at 80 °C in vacuum oven overnight. Circular discs of about 12 mm diameter with active mass loading of 6–8 mg cm^{-2} were punched out of the slurry-coated current collector and acted as the cathode. Cell assembly was carried out in a He-filled glovebox using 2325-type coin cells. A lithium metal chip was used as the anode, a solution of 1 mol $LiPF_6$ in EC : DMC (1 : 1) organic solvents as the electrolyte and a Celgard 2325 membrane as a separator. The electrochemical tests were performed on a VMP multichannel potentiostat (Bio-Logic). For *ex situ* XAS measurements, cells were disassembled in the glovebox to recover the electrode, which were rinsed with DMC to remove the residual electrolyte. After drying, the electrodes were sandwiched between the adhesive-coated Kapton tapes and sealed in the Mylar bag. Individually sealed samples were further placed into the airtight Mylar bag, sealed inside the glovebox and transported to the experimental stations for measurements. For comparison, endmember references ε-$VOPO_4$ and ε-$LiVOPO_4$ were prepared using hydrothermal[37] and sol–gel syntheses, respectively. ε-Li_2VOPO_4 reference was obtained by chemical lithiation of ε-$LiVOPO_4$. About 1 : 1 molar ratio of butyl-lithium (tiny excess butyl-lithium for practical operations) and ε-$LiVOPO_4$ was mixed in hexane and stirred for 3 days. The chemically lithiated product was rinsed with hexane for 3 times and collected with filtration. All mixing, stirring and sample collection carried out inside the He-filled glovebox to avoid exposure to air. Phase purity of all references was confirmed by X-ray diffraction.

XAS measurements were carried out using the synchrotron facilities of Advanced Photon Source (APS) in USA and Diamond Light Source (DLS) in UK. Operando investigation was carried out at beamline 5BM of APS using the modified coin cell set-up described elsewhere,[38] while the rate-dependent *ex situ* investigation was performed at beamlines 9BM and 20BM of APS and beamline 18B of DLS. Measurements were carried out in the transmission mode using the Si(111) double crystal monochromator and an unfocussed incident beam. Specific details about each of the beamlines are reported in the ESI.† Absolute energy calibration of the monochromator was carried out by measuring reference foil of pure V simultaneously with the sample. Gas-filled ionization chambers were used to record intensities of the incident beam and the beam transmitted through the sample and the reference foil. All scans were energy-calibrated with respect to the first peak in the derivative spectrum of pure V. Data processing was carried out as prescribed elsewhere,[39] using the software ATHENA of the package IFEFFIT.[40] The normalized component of the EXAFS signal was converted from energy to wavenumber and the resultant $\chi(k)$ signal was multiplied with k,[3] Fourier-transformed and left uncorrected for a phase shift. A theoretical $\chi(k)$ function was generated by performing *ab initio* calculations on relevant structural models using the code FEFF8.2 [41] and least-square fitted to data using the software ARTEMIS of the package IFEFFIT.[40]

Results

Fig. 1 illustrates the voltage profiles of ε-$LiVOPO_4$ between 1.6–4.5 V using different rates. The capacities obtained during the first discharge to 1.6 V and following charge up to 4.5 V are tabulated in Table 1. Irrespective of rates, full capacity corresponding to insertion of 1Li (*i.e.*, 153 mA h g^{-1} calculated based on the molar mass of ε-Li_2VOPO_4) is achieved during the first discharge to 1.6 V. Excluding some hysteresis, charging back to 3.5 V also delivers nearly-full capacity at all rates, except at C/100 which delivers slightly higher capacity (Table 1). The material retains similar voltage profiles at all rates with a gradually increasing 4.0 V-plateau at slower rates, revealing kinetic limitations of the high-voltage region. Again, a deviation is observed at C/100, where a step connecting the 2.5 V- and 4.0 V-plateaus becomes more sloping, delivering excess capacity.

In order to track the reaction mechanism of ε-$LiVOPO_4$, operando XAS measurements were carried out. The cell was first discharged using a rate of C/20 (1C = 153 mA g^{-1} assumed) and

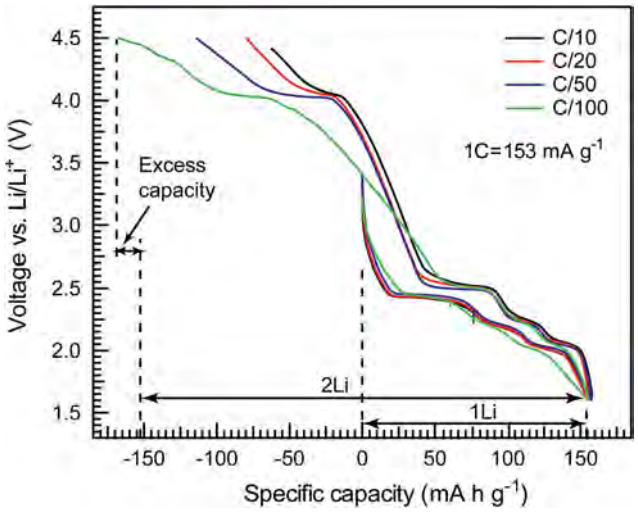

Fig. 1 Voltage profiles of ε-$LiVOPO_4$ during first discharge to 1.6 V and subsequent charge to 4.5 V using different rates.

Table 1 Specific capacities obtained during the first discharge of ε-$LiVOPO_4$ to 1.6 V and subsequent charge up to 4.5 V under different rate conditions

	Specific capacity (mA h g^{-1})			
Cycling rate	Dis. 1.6 V	Chg. 1.6–3.5 V	Chg. 3.5–4.5 V	Total@4.5 V
C/10	158	145	76	221
C20 + 10 h CV	156	147	115[a]	262
C/50	157	149	125	274
C/100	155	162	159	321

[a] 88 mA h g^{-1} of constant-current charging at C/20 and 27 mA h g^{-1} of constant-voltage holding for 10 h at 4.5 V.

data collected for various predetermined states of discharge down to 1.6 V. At each state, the cell was held at the constant-voltage until the current reduced to minimum and then data acquired (Fig. 2a). The normalized absorption spectra in Fig. 2c show a gradual shift in the position of the main edge towards lower energy and a reduction in the intensity of the pre-edge peak during discharge. The total of 171 mA h g^{-1} obtained during discharge to 1.6 V exceeds the theoretical value 153 mA h g^{-1} for insertion of 1Li in ε-$LiVOPO_4$. Despite this, the pre-edge region does not fully evolve to that of the ε-Li_2VOPO_4 reference. This disagreement between the inserted charge and evolved V valence evidences side reactions in the low-voltage region.

Subsequent charging to an upper cut-off voltage of 4.5 V was carried out at a much faster rate of C/4, followed by a constant-voltage step of 8 h (Fig. 2b). The total charge capacity of 290 mA h g^{-1} (the sum of 232 mA h g^{-1} obtained from constant-current charging at C/4 and 58 mA h g^{-1} from constant-voltage holding) corresponds to ~95% of the theoretical capacity 305 mA h g^{-1} for extraction of 2Li. Correspondingly, the V K-edge of the material is expected to nearly fully evolve to that of the ε-$VOPO_4$ reference. Quite contrarily, the main V K-edge is positioned in-between those of the pristine material and ε-$VOPO_4$ reference, with a significant contribution from the pristine material as evident in the pre-edge region (Fig. 2d). Once again, the disagreement between the extracted charge and evolved V valence evidences side reactions in the high-voltage region, but with significantly higher contributions than in the low-voltage region.

To develop better insight into the conditions promoting side reactions, rate-dependent *ex situ* XAS investigation was carried out. The normalized V K-edge absorption spectra of ε-$LiVOPO_4$ samples discharged/charged using different rates are presented in ESI Fig. S2.† For the sake of clarity and ease of comparison, the pre-edge regions and EXAFS data of these samples are presented here in Fig. 3. As observed during operando XAS measurements, none of the *ex situ* samples discharged to 1.6 V show complete evolution of their V valence to 3+ (Fig. 3a), though full capacity corresponding to insertion of 1Li was achieved at all rates (Table 1). EXAFS data also show that the local structure of discharged samples is very similar yet not fully evolved to that of the ε-Li_2VOPO_4 reference (Fig. 3d). Interestingly, the disagreement increases at slower rates, which is opposite to what would be expected if the reactions were kinetically-limited. Similar trend is observed for samples charged back to 3.5 V, with all of them delivering nearly full capacity corresponding to extraction of 1Li (Table 1), but only those charged at relatively faster rates of C/10 and C/20 + 10 h CV show more complete oxidation of V^{3+} to V^{4+} (Fig. 3b) and evolution of local structure back to that of the pristine ε-$LiVOPO_4$ (Fig. 3e). These observations indicate that slower rates tend to promote more side reactions in the low-voltage region. As shown in Fig. 3c, all samples charged to 4.5 V demonstrate mixed contributions from the pristine ε-$LiVOPO_4$ and delithiated ε-$VOPO_4$ phases, with the contribution of ε-$VOPO_4$ phase increasing at slower rates. Correspondingly, the EXAFS data of these samples represent the average local structure of both ε-$LiVOPO_4$ and ε-$VOPO_4$ phases. These results confirm kinetic limitations of the high-voltage region as also evidenced in the voltage profiles.

Based on qualitative similarities, EXAFS data of the samples discharged to 1.6 V and charged to 3.5 V were explained based on the triclinic structure of ε-Li_2VOPO_4 [27] and ε-$LiVOPO_4$,[42] respectively. As shown in Fig. S3a,† EXAFS data of ε-$VOPO_4$ and ε-$LiVOPO_4$ have no distinctly different characteristic features, except that improved crystal symmetry of monoclinic ε-$VOPO_4$ [43] and therefore, less distorted local structure in comparison to triclinic ε-$LiVOPO_4$ gives rise to more intense EXAFS peaks for ε-$VOPO_4$. Under these circumstances and due to high correlations among various fitting parameters,[44,45] estimation of relative fractions of ε-$VOPO_4$ and ε-$LiVOPO_4$ phases samples charged to charged 4.5 V based on EXAFS fitting would not be reliable. Notably, EXAFS data of samples charged to 4.5 V were best explained based on ε-$LiVOPO_4$ structure, since the average local structure of both ε-$LiVOPO_4$ and ε-$VOPO_4$ phases may appear closer to that of highly distorted ε-$LiVOPO_4$. A good agreement between the data and fits for all samples can be seen in Fig. S4.† Details about EXAFS fitting procedure are presented in ESI.†

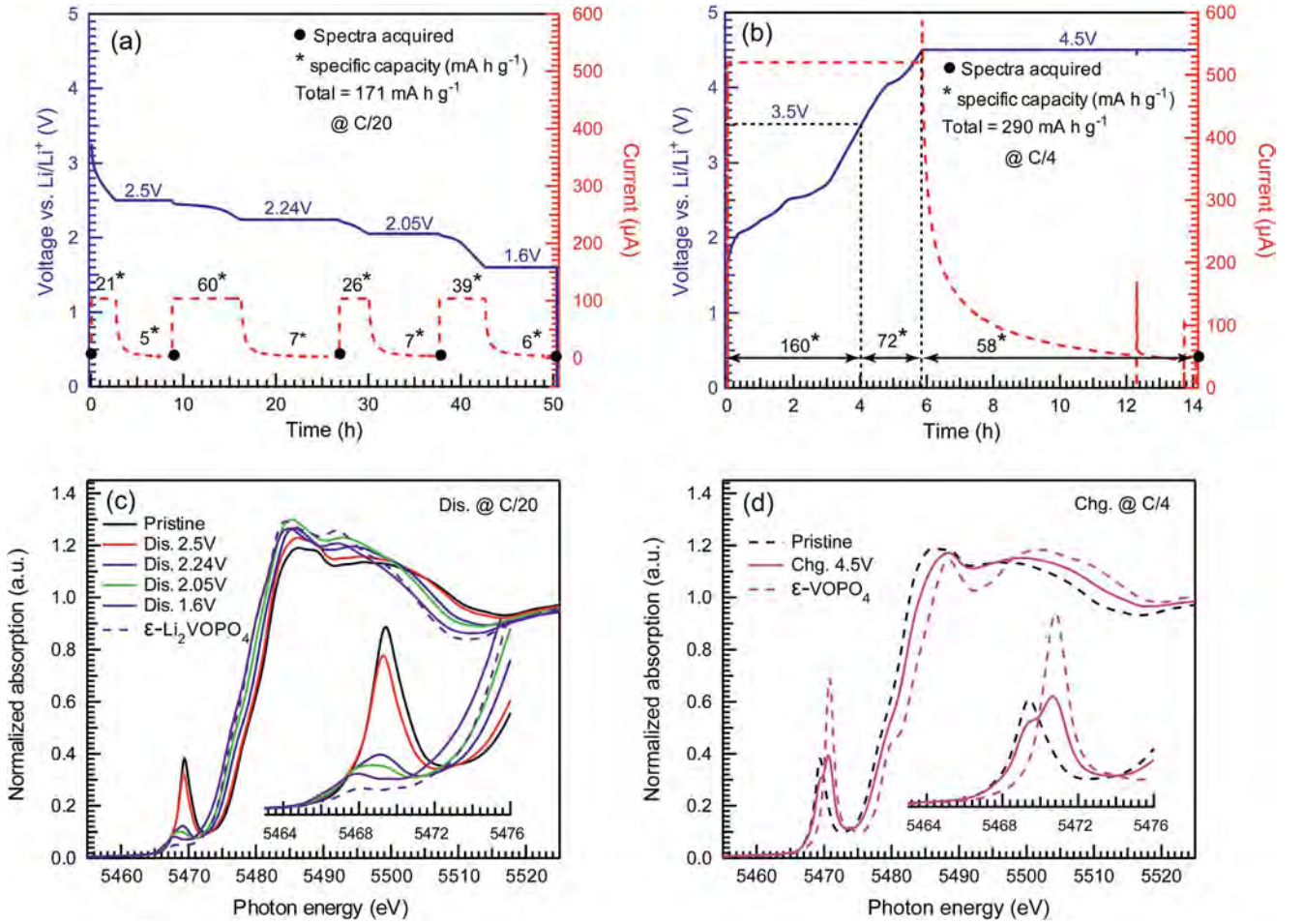

Fig. 2 Variation in the cell voltage and current during operando XAS measurements upon (a) discharge to 1.6 V at C/20 and (b) subsequent charge to 4.5 V at C/4. The normalized V K-edge absorption spectra of ε-$LiVOPO_4$ for various states of discharge and charge are presented in (c) and (d), respectively, with the inset showing an enlarged pre-edge region of these spectra.

Fig. 4 shows variation in the average V–O bond length obtained by EXAFS fitting of ε-$LiVOPO_4$ samples discharged/charged using different rates. The average V–O bondlength of the starting material is in good agreement with that of the ε-$LiVOPO_4$ reference. Electrochemical insertion of Li into ε-$LiVOPO_4$ causes reduction of V^{4+} to V^{3+} and consequently, disappearance of the short vanadyl bond length. As a result, the average V–O bond length for samples discharged to 1.6 V increases and becomes similar to that of ε-Li_2VOPO_4 reference at all rates, except at C/100 which shows some deviation. Li extraction upon charging back to 3.5 V causes oxidation of V^{3+} back to V^{4+}, which in turn, gives rise to the short vanadyl bond length. Accordingly, the average V–O bond length for samples charged to 3.5 V decreases back and becomes similar to that of the ε-$LiVOPO_4$ reference. However, the average V–O bond length of the samples charged to 4.5 V appears to be scattered around those of ε-$LiVOPO_4$ and ε-$VOPO_4$ references. The sample charged at the slowest rate of C/100 has its average V–O bond length closer to that of ε-$VOPO_4$ reference, while the sample charged at C/10 has its average V–O bond length closer to that of ε-$LiVOPO_4$ reference. Thus, changes in the average V–O bond length of different discharged/charged samples directly correlate with the observed changes in the pre-edge region of these samples.

Unlike EXAFS data, the spatially-resolved contributions of V^{4+} and V^{5+} in the pre-edge region of samples charged to 4.5 V and the availability of phase pure ε-$VOPO_4$ reference permitted for the estimation of relative fractions of V^{4+} and V^{5+} using the Linear-combination fitting (LCF) approach (see Fig. S5b†). Details about LCF are reported in ESI.† The fraction of V^{5+} detected by LCF as summarized in Table 2 clearly shows that slower rates and/or constant-voltage steps give rise to higher fractions of V^{5+} upon charge, but there remains a huge difference between the observed and expected fraction of V^{5+} at all rates. An estimate of capacity based on the observed fraction of V^{5+}, which corresponds to the true electrochemical deintercalation and its comparison with the observed capacity in Table 3 reveals significant contributions from side reactions in the high-voltage region, irrespective of rates, as illustrated in Fig. 5. Similar LCF analysis of samples discharged to 1.6 V revealed only ~10% of residual V^{4+} at C/10 and C/20 + 10 h, which increased to ~14% at slower rates of C/50 and C/100. This corresponds to the unaccounted capacity of 15–20 mA h g^{-1},

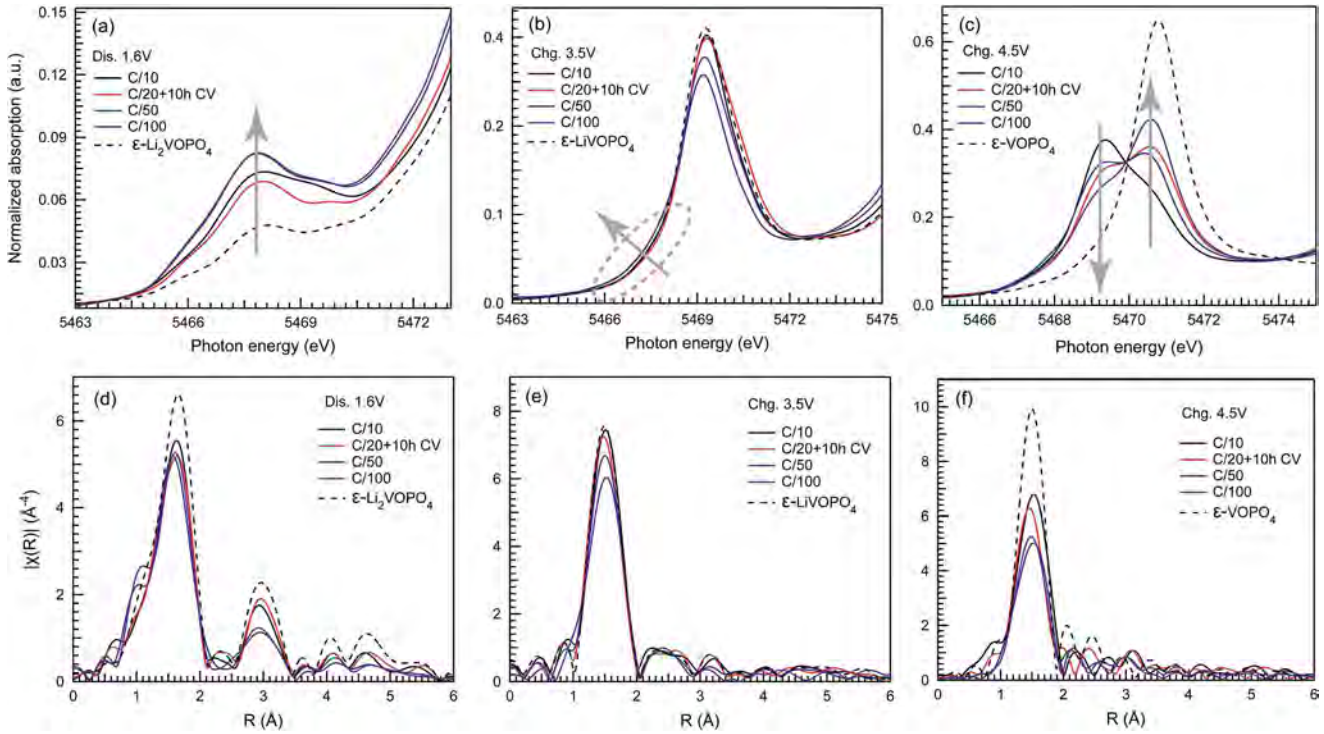

Fig. 3 Comparison of the pre-edge regions (top) and EXAFS signals (bottom) of ε-$LiVOPO_4$ samples discharged to 1.6 V (a and d), charged to 3.5 V (b and e) and charged to 4.5 V (c and f) using different rates.

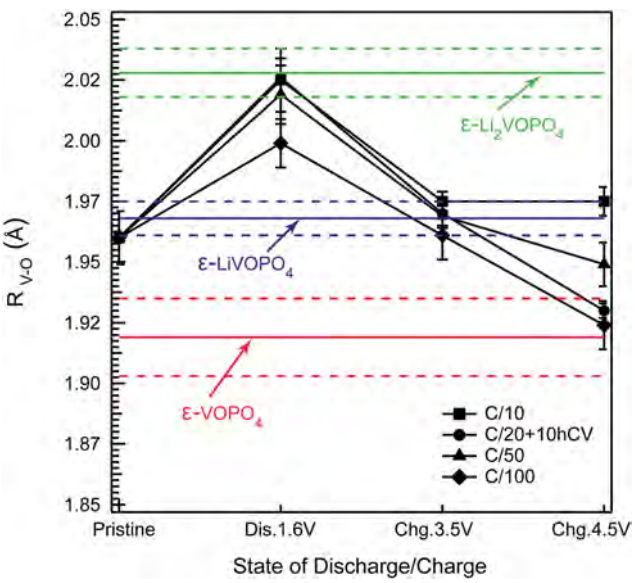

Fig. 4 Variation in the average V–O (metal–ligand) bond length of ε-$LiVOPO_4$ samples electrochemically discharged/charged using different rates. The solid horizontal lines indicate the average V–O bond length of chemically prepared endmember phases and the dotted horizontal lines indicate the uncertainties of the fitted values.

which is significantly smaller in comparison to that observed in the high-voltage region.

To investigate the implications of side reactions on the long-term cycling performance of the material, discharged/charged samples were examined after 10 cycles. As can be seen in Fig. 6a, the voltage profiles in the 1st and 10th cycles remain quite similar and so does the capacity delivered, indicating stable cycling performance of the material. The pre-edge region of samples discharged to 1.6 V on the 1st and 10th cycles evolve identically and do not show complete reduction to V^{3+}. However, the sample charged to 4.5 V on the 10th cycle clearly exhibits higher V^{5+} in comparison to that observed in the 1st cycle for the same capacity delivered. These results indicate improved participation of the high-voltage V^{5+}/V^{4+} redox upon cycling. In other words, side reactions of high-voltage region gradually diminish upon cycling.

Table 2 Comparison of the expected (Exp.) fraction of V^{5+} based on electrochemistry with that observed (Obs.) based on LCF of the pre-edge region for samples charged to 4.5 V using different rates

Cycling rate	Frac. of V^{5+} (Exp.)[a]	Frac. of V^{5+} (Obs.)
C/10	0.50	0.11(1)
C20 + 10 h CV	0.75	0.39(1)
C/50	0.82	0.35(1)
C/100	1.0	0.53(1)

[a] Observed charge capacity from 3.5 V to 4.5 V in Table 1 divided by the theoretical capacity for 1Li (*i.e.*, 153 mA h g^{-1}).

Discussion

ε-$LiVOPO_4$ is a pseudo one-dimensional Li-ion conductor with low electronic conductivity.[21,31] Thus, smaller particle size, leading to shorter Li-ion diffusion pathways and higher specific

Table 3 Comparison between the observed and expected capacities during charge up to 4.5 V under different rate conditions

	Specific charge capacity (mA h g^{-1})			
Cycling rate	1.6 V to 3.5 V (Obs.)	3.5 V to 4.5 V (Exp.)[a]	3.5 V to 4.5 V (Obs.)[b]	Unaccounted capacity[c]
C/10	145	17(2)	76	59
C20 + 10 h CV	147	60(2)	115	55
C/50	149	54(2)	125	71
C/100	162	81(2)	159	78

[a] = Observed fraction of V^{5+} (see Table 2) multiplied by the theoretical capacity for 1Li (*i.e.*, 153 mA h g^{-1}). [b] = Observed charge capacity from 3.5–4.5 V (see Table 1). [c] = b − a.

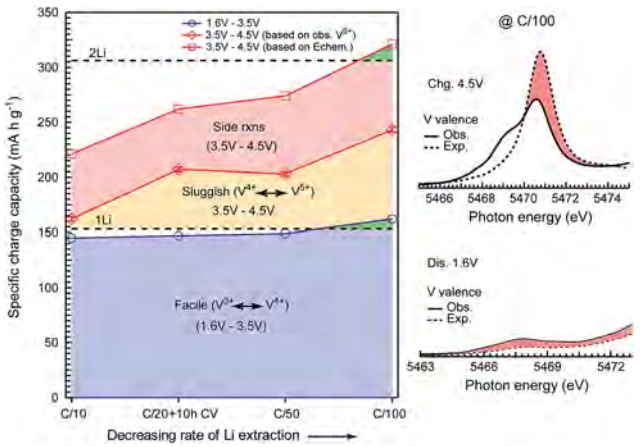

Fig. 5 Observed capacity and V valence during charge reveal facile V^{4+}/V^{3+} redox in the low-voltage region and sluggish V^{5+}/V^{4+} redox with pronounced side reactions contributions in the high-voltage region. This is shown by higher discrepancy between the observed (Obs.) and expected (Exp.) V valence for the sample charged to 4.5 V than for the sample discharged to 1.6 V at the slowest rate of C/100.

surface area together with improved particle-carbon contacts are recommended.[11,13,17,21] Consequently, HEBM is an indispensable step in solid-state synthesize of ε-$LiVOPO_4$.[34] However, our recent study showed that HEBM of ε-$LiVOPO_4$ with carbon also induces some reduction of V^{4+} to V^{3+} in addition to deteriorating bulk crystallinity of the material.[34] Since the starting material is a stoichiometric ε-$LiVOPO_4$, it is reasonable to assume that the HEBM-induced reduction of V^{4+} may be associated with oxygen loss, giving rise to high concentrations of oxygen vacancies in active electrode particles. It has been shown that electrochemical insertion of Li into ε-$LiVOPO_4$ is kinetically favored compared to extraction of Li from ε-$LiVOPO_4$.[31] Under these circumstances and despite achieving the full capacity, the observed discrepancy in the V valence indicates that a small portion of total discharge capacity at 1.6 V can be attributed to reactions other than the true electrochemical intercalation, such as the formation of cathode-electrolyte interface (CEI) as reported previously.[30] Interestingly, slower rates (C/50 and C/100) and constant-voltage steps do not necessarily facilitate the complete reduction of V^{4+} to V^{3+}, but likely promote thicker and unstable CEI, reaching or exceeding the theoretical capacity but with higher residual V^{4+} in comparison to faster rates. These results highlight the role of HEBM-induced structural distortions in limiting the otherwise facile insertion of full 1Li into ε-$LiVOPO_4$, since such limitations have not been encountered upon electrochemical lithiation of ε-$VOPO_4$ obtained by HEBM-free hydrothermal synthesis.[37] Moreover, in the absence of rate-

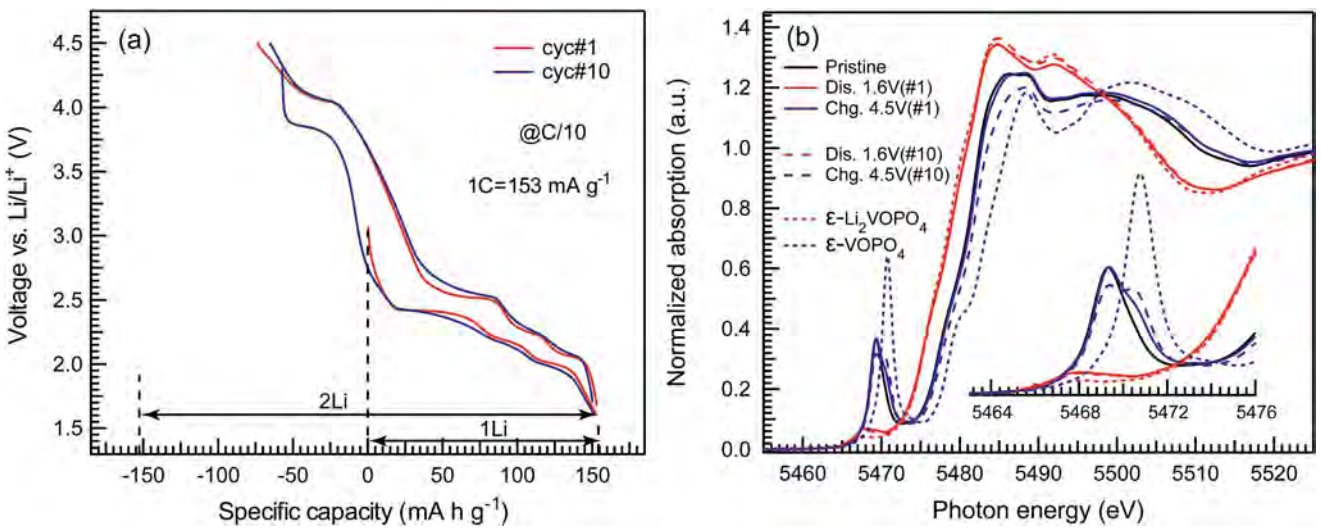

Fig. 6 (a) Voltage profiles and (b) the normalized V K-edge absorption spectra of ε-$LiVOPO_4$ samples discharged to 1.6 V and charged to 4.5 V in the 1st and 10th cycles.

dependent investigation and ε-Li_2VOPO_4 endmember reference presented herein, the side reactions of low-voltage region would have gone undetected as in the previous studies.[22,31,32]

Li extraction from ε-Li_2VOPO_4 during subsequent charge up to 3.5 V is expected to proceed *via* simultaneous oxidation of V^{3+} to V^{4+}, thus reforming the original ε-$LiVOPO_4$. Due to favorable kinetics of the low-voltage region, nearly full capacity corresponding to extraction of 1Li is obtained during charge to 3.5 V at all rates (Table 1). However, the presence of some residual V^{3+} at slower rates of C/50 and C/100, despite achieving the full capacity, suggests that a small portion of charge capacity at 3.5 V may come from partial decomposition of unstable CEI.[30] These results reiterate that slower rates do not necessarily overcome the kinetic limitations imposed by HEBM, but rather promote more side reactions in the low-voltage region.

Further Li extraction from ε-$LiVOPO_4$ during charge between 3.5 V–4.5 V is confronted by sluggish kinetics.[31] Consequently, operando XAS, where charging was carried out at a much faster rate of C/4, involved a constant-voltage step at 4.5 V (Fig. 2b). The total 130 mA h g^{-1} obtained between 3.5–4.5 V (*i.e.*, constant-current and constant-voltage steps combined) corresponds to the extraction of 0.85Li. Accordingly, the expected fraction of V^{5+} should be 0.85, assuming the pure electrochemical deintercalation reactions (*i.e.*, extracted Li^+ being charge-compensated by oxidation of V^{4+} to V^{5+}). However, the observed fraction of V^{5+} as 0.46 is much smaller (Fig. S6†), indicating significant contributions from side reactions. In order to assess if the constant-voltage holding at 4.5 V was responsible for side reactions, we considered only 72 mA h g^{-1} obtained during constant-current charging between 3.5–4.5 V, which corresponds to the extraction of 0.47Li and agrees well with the observed fraction of V^{5+}. However, it appears unrealistic when compared with the fraction of V^{5+} observed as 0.11 upon charging at C/10 (Table 2). Since slower rates mitigate sluggish kinetics, the observed fraction of V^{5+} at C/4 cannot be higher than at C/10, unless a constant-voltage step employed at the end of constant-current charging of C/4 is also contributing towards electrochemical deintercalation reactions. Similar trend is observed for samples charged at C/20 + 10 h CV and C/50, as both these samples demonstrated comparable fractions of V^{5+} (Table 2). These results suggest that the total capacity during charge between 3.5–4.5 V, with or without constant-voltage steps, has contributions from both the sluggish electrochemical deintercalation processes and interfacial side reactions. In fact, these two processes are so closely intertwined in the high-voltage region that they cannot be distinguished by mere examination of voltage profiles. For instance, voltage profiles during charge at C/10, C/20, C/50 look alike with a gradually increasing 4.0 V-plateau with decreasing rates, as expected for the kinetically sluggish V^{5+}/V^{4+} redox. The difference becomes noteworthy only at extremely slow rate of C/100, which also delivers excess capacity (Fig. 1). Nonetheless, all of them have contribution that is unaccounted for the V^{5+}/V^{4+} redox and therefore, originating from interfacial side reactions (Fig. 5).

The observed unaccounted capacity during charge between 3.5–4.5 V largely remains unchanged with decreasing rates (Fig. 5). As a result, it does not appear to be a capacitive contribution, which is otherwise shown to decrease at slower rates in case of ultrathin $VOPO_4$ nanosheets.[46] This gives rise to another speculation about the stability of electrochemically delithiated phase ε-$VOPO_4$ in contact with the electrolyte, particularly, since ε-$VOPO_4$ is a commercial catalyst. However, our recent report on hydrothermally-synthesized (ball milling-free approach) ε-$VOPO_4$ with highly crystalline primary particles of ~100–200 nm demonstrated the full theoretical capacity for reversible intercalation of 2Li without any indication of side reactions, since the observed V valence directly correlated with the charge inserted/extracted.[37] This report confirms that the observed side reactions in case of solid-state-synthesized ε-$LiVOPO_4$ are neither intrinsic to vanadyl phosphates nor due to a capacitive contribution, but are the consequences of sluggish kinetics compounded by the HEBM-induced structural distortions and/or defects (*i.e.*, oxygen vacancies). Slower rates and constant-voltage steps do alleviate kinetic barriers of the high-voltage region to some extent, but longer exposures between the active electrode particles and electrolyte inadvertently result into interfacial side reactions (Fig. 5). Identifying these side reactions is beyond the scope of the present work and should be the subject of future investigation. As such, understanding the role of interfacial side reactions remains a major challenge for the battery community. The dynamic nature of these reactions which involve lighter species that are prone to radiation damage pose additional complexity and calls for *in situ/operando* investigation, preferably using soft-XAS and specially designed cell architecture, as demonstrated by Liu *et al.*[47] Furthermore, the experimental data need to be complemented by theoretical simulations (*i.e.* beyond DFT calculations).

Interfacial side reactions could also be, to some extent, self-limiting in nature. This can be observed by an improved contribution of the V^{5+}/V^{4+} redox upon cycling in Fig. 6. It is likely that species deposited on active electrode particles as a result of interfacial side reactions may passivate the electrode surface for further side reactions upon cycling, albeit at a cost of increased cell impedance. In fact, one plausible way to mitigate side reactions could be to prevent direct contacts between active particles and the electrolyte using surface coatings.[34] Another approach may involve partial restoration of material's crystallinity using post-annealing treatments. However, a careful control over annealing temperature and time must be necessary to avoid excessive grain growth, which could be detrimental due to poor transport properties of the material. While both these approaches may mitigate but not suppress side reactions completely, preserving the bulk crystallinity and defect-free structure of active material through nanoengineering, as demonstrated for highly crystalline, nano-sized ε-$VOPO_4$,[37] seems to be the only remedy.

Conclusions

In summary, our findings reveal the role of HEBM in limiting the true multi-electron redox in ε-$LiVOPO_4$. Structural distortions caused by HEBM restrict the otherwise facile insertion of second Li into ε-$LiVOPO_4$ during discharge, though to a limited

extent due to favorable kinetics of the low-voltage region. On the other hand, inherently sluggish kinetics of the high-voltage region are further compounded by HEBM-induced disorder/defects and pave the way for significant side reaction contributions, irrespective of cycling conditions. Thus, the element-selective nature of XAS provides a unique opportunity to monitor the electrochemical processes in Li-ion batteries and separate the contributions of pure intercalation/deintercalation reactions from those of side reactions.

Author contributions

J. R., L. F. J. P., N. C., and M. S. W. conceived the experiments. Y. S. performed electrochemical testing, while F. O. and H. Z. assisted in preparing ex-situ samples and phase pure end-member references. J. R., M. J. Z., J. F., K. M. W., K. W. C. and J. D. performed experiments with the assistance of T. W., G. C., and M. B. J. R. analyzed the data and prepared the manuscript with contributions from all authors. L. F. J. P. supervised the project.

Conflicts of interest

There are no conflicts of interest to declare.

Acknowledgements

This work was supported as part of the NorthEast Center for Chemical Energy Storage (NECCES), an Energy Frontier Research Center funded by the U.S. Department of Energy, Office of Science, Basic Energy Sciences under Award# DE-SC0012583. This research used resources of the Advanced Photon Source, a U.S. Department of Energy (DOE) Office of Science User Facility operated for the DOE Office of Science by Argonne National Laboratory under Contract No. DE-AC02-06CH11357. The authors gratefully acknowledge Dr Qing Ma for his assistance during XAS experiments at beamline 5BM of Advanced Photon Source. The authors also acknowledge Diamond Light Source for access to beamline B18 (Proposal# SP18423) that contributed to the results presented here. M. J. Z. was supported as part of the Multidisciplinary GAANN in Smart Energy Materials, a Graduate Areas of National Need, funded by the U.S. Department of Education, under Award# P200A150135. The authors are grateful to Dr Matthew Wahila for inspiring Table of Contents graphics and cover page artworks.

Notes and references

1 G. Amatucci, *J. Electrochem. Soc.*, 1996, **143**, 1114.
2 A. Padhi, K. Nanjundaswamy and J. Goodenough, *J. Electrochem. Soc.*, 1997, **144**, 1188.
3 M. Whittingham, *Chem. Rev.*, 2004, **104**, 4271–4301.
4 T. Ohzuku and Y. Makimura, *Chem. Lett.*, 2001, **30**, 642–643.
5 M. Guilmard, L. Croguennec and C. Delmas, *Chem. Mater.*, 2003, **15**, 4484–4493.
6 K. Luo, M. Roberts, R. Hao, N. Guerrini, D. Pickup, Y.-S. Liu, K. Edström, J. Guo, A. Chadwick, L. Duda and P. Bruce, *Nat. Chem.*, 2016, **8**, 1–17.
7 A. Grimaud, W. T. Hong, Y. Shao-Horn and J.-M. Tarascon, *Nat. Mater.*, 2016, **15**, 121–126.
8 G. Assat, D. Foix, C. Delacourt, A. Iadecola, R. Dedryvère and J.-M. Tarascon, *Nat. Commun.*, 2017, **8**, 1–12.
9 G. Assat and J.-M. Tarascon, *Nat. Energy*, 2018, **3**, 1–14.
10 S. Lim, J. Vaughey, W. Harrison, L. Dussack, A. Jacobson and J. Johnson, *Solid State Ionics*, 1996, **84**, 219–226.
11 T. Kerr, J. Gaubicher and L. Nazar, *Electrochem. Solid-State Lett.*, 1999, **3**, 460.
12 J. Gaubicher, T. Mercier, Y. Chabre, J. Angenault and M. Quarton, *J. Electrochem. Soc.*, 1999, **146**, 4375–4379.
13 N. Dupré, J. Gaubicher, T. Mercier, G. Wallez, J. Angenault and M. Quarton, *Solid State Ionics*, 2001, **140**, 209–221.
14 B. Azmi, T. Ishihara, H. Nishiguchi and Y. Takita, *J. Power Sources*, 2003, **119–121**, 273–277.
15 M. Whittingham, Y. Song, S. Lutta, P. Zavalij and N. Chernova, *J. Mater. Chem.*, 2005, **15**, 3362.
16 Y. Song, P. Zavalij and M. Whittingham, *J. Electrochem. Soc.*, 2005, **152**, A721.
17 B. Azmi, T. Ishihara, H. Nishiguchi and Y. Takita, *J. Power Sources*, 2005, **146**, 525–528.
18 M. Whittingham, *MRS Bull.*, 2008, **33**, 411–419.
19 N. Chernova, M. Roppolo, A. Dillon and M. Whittingham, *J. Mater. Chem.*, 2009, **19**, 2526.
20 M. Ren, Z. Zhou, L. Su and X. Gao, *J. Power Sources*, 2009, **189**, 786–789.
21 Y. Yang, H. Fang, J. Zheng, L. Li, G. Li and G. Yan, *Solid State Sci.*, 2008, **10**, 1292–1298.
22 C. J. Allen, Q. Jia, C. N. Chinnasamy, S. Mukerjee and K. M. Abraham, *J. Electrochem. Soc.*, 2011, **158**, A1250.
23 K. Saravanan, H. Lee, M. Kuezma, J. Vittal and P. Balaya, *J. Mater. Chem.*, 2011, **21**, 10042.
24 J.-M. Ateba Mba, C. Masquelier, E. Suard and L. Croguennec, *Chem. Mater.*, 2012, **24**, 1223–1234.
25 K. Harrison and A. Manthiram, *Chem. Mater.*, 2013, **25**, 1751–1760.
26 Z. Chen, Q. Chen, L. Chen, R. Zhang, H. Zhou, N. Chernova and M. Whittingham, *J. Electrochem. Soc.*, 2013, **160**, A1777–A1780.
27 M. Bianchini, J. Ateba-Mba, P. Dagault, E. Bogdan, D. Carlier, E. Suard, C. Masquelier and L. Croguennec, *J. Mater. Chem. A*, 2014, **2**, 10182.
28 K. Harrison, C. Bridges, C. Segre, C. D. Varnado, D. Applestone, C. Bielawski, M. P. Paranthaman and A. Manthiram, *Chem. Mater.*, 2014, **26**, 3849–3861.
29 G. He, C. Bridges and A. Manthiram, *Chem. Mater.*, 2015, **27**, 6699–6707.
30 N. Quackenbush, L. Wangoh, D. Scanlon, R. Zhang, Y. Chung, Z. Chen, B. Wen, Y. Lin, J. Woicik, N. Chernova, S. P. Ong, M. Whittingham and L. Piper, *Chem. Mater.*, 2015, **27**, 8211–8219.
31 Y.-C. Lin, B. Wen, K. Wiaderek, S. Sallis, H. Liu, S. Lapidus, O. Borkiewicz, N. Quackenbush, N. Chernova, K. Karki,

F. Omenya, P. Chupas, L. Piper, M. Whittingham, K. Chapman and S. Ong, *Chem. Mater.*, 2016, **28**, 1794–1805.
32 L. Wangoh, S. Sallis, K. Wiaderek, Y.-C. Lin, B. Wen, N. Quackenbush, N. Chernova, J. Guo, L. Ma, T. Wu, T.-L. Lee, C. Schlueter, S. Ong, K. Chapman, M. Whittingham and L. Piper, *Appl. Phys. Lett.*, 2016, **109**, 053904.
33 E. Boivin, J.-N. Chotard, M. Ménétrier, L. Bourgeois, T. Bamine, D. Carlier, F. Fauth, C. Masquelier and L. Croguennec, *J. Phys. Chem. C*, 2016, **120**, 26187–26198.
34 Y. Shi, H. Zhou, I. Seymour, S. Britto, J. Rana, L. Wangoh, Y. Huang, Q. Yin, P. Reeves, M. Zuba, Y. Chung, F. Omenya, N. Chernova, G. Zhou, L. Piper, C. Grey and M. Whittingham, *ACS Omega*, 2018, **3**, 7310–7323.
35 B. Wen, Q. Wang, Y. Lin, N. Chernova, K. Karki, Y. Chung, F. Omenya, S. Sallis, L. Piper, S. Ong and M. Whittingham, *Chem. Mater.*, 2016, **28**, 3159–3170.
36 M. Whittingham, C. Siu and J. Ding, *Acc. Chem. Res.*, 2018, **51**, 258–264.
37 C. Siu, I. Seymour, S. Britto, H. Zhang, J. Rana, J. Feng, F. Omenya, H. Zhou, N. Chernova, G. Zhou, C. Grey, L. Piper and M. Whittingham, *Chem. Commun.*, 2018, **54**, 7802–7805.
38 J. Rana, S. Glatthaar, H. Gesswein, N. Sharma, J. Binder, R. Chernikov, G. Schumacher and J. Banhart, *J. Power Sources*, 2014, **255**, 439–449.
39 S. Kelly, D. Hesterberg, B. Ravel, A. L. Ulery and R. Drees, *Methods Soil Anal. - Part 5. Mineral. Methods*, Soil Science Society of America, Madison, WI, USA, 2008, pp. 387–464.
40 B. Ravel and M. Newville, *J. Synchrotron Radiat.*, 2005, **12**, 537–541.
41 A. Ankudinov, B. Ravel, J. Rehr and S. Conradson, *Phys. Rev. B*, 1998, **58**, 7565–7576.
42 A. Lavrov, V. Nikolaev, G. Sadikov and M. Porai Koshits, *Dokl. Akad. Nauk SSSR*, 1982, **266**, 343–346.
43 F. Girgsdies, W. Dong, J. Bartley, G. Hutchings, R. Schlögl and T. Ressler, *Solid State Sci.*, 2006, **8**, 807–812.
44 B. Ravel and S. Kelly, *AIP Conf. Proc.*, 2007, **882**, 150–152.
45 J. Rana, M. Stan, R. Kloepsch, J. Li, G. Schumacher, E. Welter, I. Zizak, J. Banhart and M. Winter, *Adv. Energy Mater.*, 2014, **4**, 1–12.
46 Y. Zhu, L. Peng, D. Chen and G. Yu, *Nano Lett.*, 2016, **16**, 742–747.
47 X. Liu, D. Wang, G. Liu, V. Srinivasan, Z. Liu, Z. Hussain and W. Yang, *Nat. Commun.*, 2013, **4**, 1–8.